Evaluation of Ordering in Single-Component and Binary Nanocrystal Superlattices by Analysis of Their Autocorrelation Functions

Stefan Pichler,[†,*] Maryna I. Bodnarchuk,[†,‡] Maksym V. Kovalenko,[†,‡] Maksym Yarema,[†] Gunther Springholz,[†] Dmitri V. Talapin,[‡] and Wolfgang Heiss[†,*]

[†]Institute of Semiconductor and Solid State Physics, University Linz, Linz, Austria and [‡]Chemistry Department, University of Chicago, Chicago, Illinois, United States.

ABSTRACT Self-assembly of colloidal nanocrystals and other nanosized building blocks has led to numerous large-scale and well-ordered superstructures. To quantify the superlattice quality we present a simple and efficient method, based on analysis of the autocorrelation function to determine characteristic order parameters for short-range and long-range ordering. This provides a feedback for further improvements of deposition techniques and self-assembly processes. To show the power of this method, it is applied to various two-dimensional ordered single component and binary nanocrystal assemblies. A quantitative comparison of the normalized long-range order parameter for various colloidal or epitaxially grown superlattice structures evidences that the long-range ordering in monodisperse colloidal superlattices by far supersedes that obtained at best by epitaxially grown quantum dots. Astonishingly, for selected binary nanocrystal superlattices the long-range ordering parameter reaches almost the same values as for single component superlattices. Besides the high sensitivity of the introduced quantification method to lattice imperfections our analysis also reveals any anisotropy in the ordering of the superlattices, which again can be quantified, for example, to identify the areas of highest quality within one specific sample.

KEYWORDS: self-assembled superlattices · nanocrystal superstructures · autocorrelation · quantification of ordering · epitaxial quantum dots

The degree of ordering in superstructures of uniform nanosized building blocks such as colloidal nanocrystals (NCs) or epitaxial quantum dots has been shown to be a key parameter to control their physical, chemical, and mechanical properties.[1−3] Ordering in epitaxial dots provides the possibility to improve their size homogeneity,[4−8] whereas for colloidal nanocrystals the challenge, for example, is to form electronic minibands by coupling their electronic states in close-packed structures.[9] A further advantage of ordering is that the positions of the individual building blocks become deterministic, making them addressable on an individual basis. The latter is of great importance in memory devices, which could be obtained by two-dimensional self-assembly of magnetic nanocrystals, each acting as a binary digital unit (bit). Self-assembly of colloidal nanocrystals during complete evaporation of their carrier solution has led to a large variety of single component[10−19] (Figure 1A) and binary superstructures[20−28] (Figures 1 B,C) with two or even three-dimensional ordering. This is driven by van der Waals interactions, as well as by dipole−dipole, Coulomb interactions, or by maximization of entropy.[23−25] To obtain ordered superstructures over larger areas, deposition techniques such as drop casting,[11,12] spin-casting,[13] Langmuir−Blodgett deposition,[14,15] and doctor blade casting[16] have been employed. For practical applications of these superstructures, however, their long-range ordering has to be improved. This requires a quantitative measure of the obtained degree of ordering as a feedback for the deposition process. While for a first qualitative inspection of NC superstructures electron microscopy is usually employed, quantifying the degree of ordering requires high effort experiments such as grazing incidence small X-ray scattering.[16−19] Alternatively, various statistical analyses of microscopy images can be performed. For colloidal particle-assemblies, commonly translational/pair correlation or bond orientational correlation functions have been computed.[19,29−33] These methods require extensive computational time when applied to large ensembles of NCs, and they rely on the knowledge of the exact coordinates of each NC centroid, which have to be found manually. Here, we suggest a much more convenient method to quantify the ordering of NC superstructures based on the analysis of their two-dimensional (2D) autocorrelation functions (ACFs). In particular, we propose a standardized procedure to generate and analyze these ACFs by using readily available software

* Address correspondence to stefan.pichler@jku.at, wolfgang.heiss@jku.at.

Received for review August 25, 2010 and accepted February 21, 2011.

Published online March 03, 2011
10.1021/nn200265e

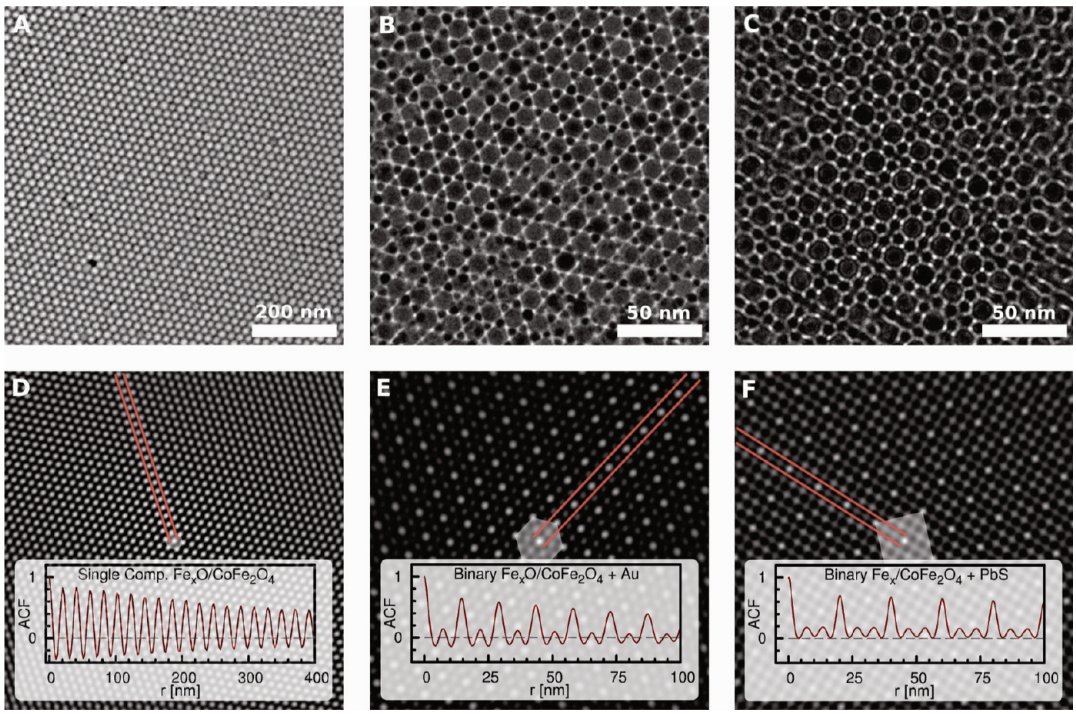

Figure 1. (A) SEM image of a single component 20 nm W/C-NC superlattice. (B) TEM images of binary superlattices of hexagonal symmetry consisting of 11 nm W/C-NC and 5.5 nm Au nanocrystals, AlB_2 structure. (C) Binary superlattice of cubic symmetry consisting of 11 nm W/C-NC and 5 nm PbS nanocrystals, $NaZn_{13}$ structure. (D−F) 2D-ACFs of the superlattices shown in panels A−C. The unit cells are indicated in gray and the line profiles of the ACFs along the red lines (the main axes of the crystals) are shown as insets. For the binary superlattices, the ACF line-profiles exhibit secondary satellite peaks.

and simple evaluation routines to deduce three characteristic order parameters of the nanoparticle assemblies that quantify the degree of short-range (κ_{sr}) and long-range (ξ_{lr}) ordering as well as anisotropy (a) of ordering. The various contributions of disorder to the characteristic properties of the ACFs are demonstrated and discussed for superlattices with well-defined artificially introduced imperfections. This yields a standardized procedure that is applied to various examples of single component and binary NC superstructures with close to perfect ordering for up to 2500 NC building blocks, demonstrating the high quantitative sensitivity of our method.

RESULTS AND DISCUSSION

Autocorrelation Functions of Different Nanocrystal Superlattices. NC superlattices show different lattice structures depending on the shape, number, and size ratio of the NC constituents as well as depending on the assembly techniques and deposition parameters.[10,21,22] This is illustrated in Figure 1 by the SEM image of a single component superlattice of 20 nm Wüstite/cobalt ferrite ($Fe_xO/CoFe_2O_4$) core−shell NCs (W/C-NCs) deposited *via* doctor blade casting on silicon substrate (Figure 1A) together with the TEM images of two binary superlattices, consisting of such W/C-NCs with 11 nm diameter combined either with 5.5 nm Au NCs forming a hexagonal (001) projection of a AlB_2-like binary superlattice (Figure 1B), or with 5 nm PbS NCs forming the topmost layer of a cubic $NaZn_{13}$ structure (Figure 1C). The 2D-ACFs of these superlattices are shown in Figures 1D−F, respectively. In general, ACFs represent the integral over a signal $s(\mathbf{x})$ times the signal shifted by a displacement vector $\mathbf{r}$, $s(\mathbf{x} + \mathbf{r})$, where in our case $s(\mathbf{x})$ represents the 2D intensity distribution of the image of the NC assembly recorded by any microscopy technique (a detailed mathematical description of the ACF is given in the Supporting Informations section). The value of the integral, normalized to the value at $\mathbf{r} = 0$, gives a measure for the self-similarity of the microscope image in dependence of the displacement vector. In particular, if for a given $\mathbf{r}$ the ACF value is high (*i.e.*, close to 1) all points in the image spaced by $\mathbf{r}$ are highly correlated, as is the case for a periodic superlattice, for example, along the main axes for distances equal to the lattice constant. For disordered structures, on the other hand, the ACF rapidly drops to zero at larger displacements because in this case the image points are no longer correlated to each other. From the ACF image center the displacement vector $\mathbf{r}$ points into all directions, giving a complete, centrosymmetric 2D-ACF. ACFs are routinely computed by using standard numerical software packages (such as Matlab and GNU Octave) and even more conveniently using microscope image analysis software (such as Gwyddion Software Package), giving the 2D-ACF $A(\mathbf{r})$ in the form of 2D-matrix/bitmap images. The symmetry of the 2D-ACFs and that of the investigated NC superlattices is always the same, for example, the 2D-ACFs of the hexagonally ordered NC superlattices in

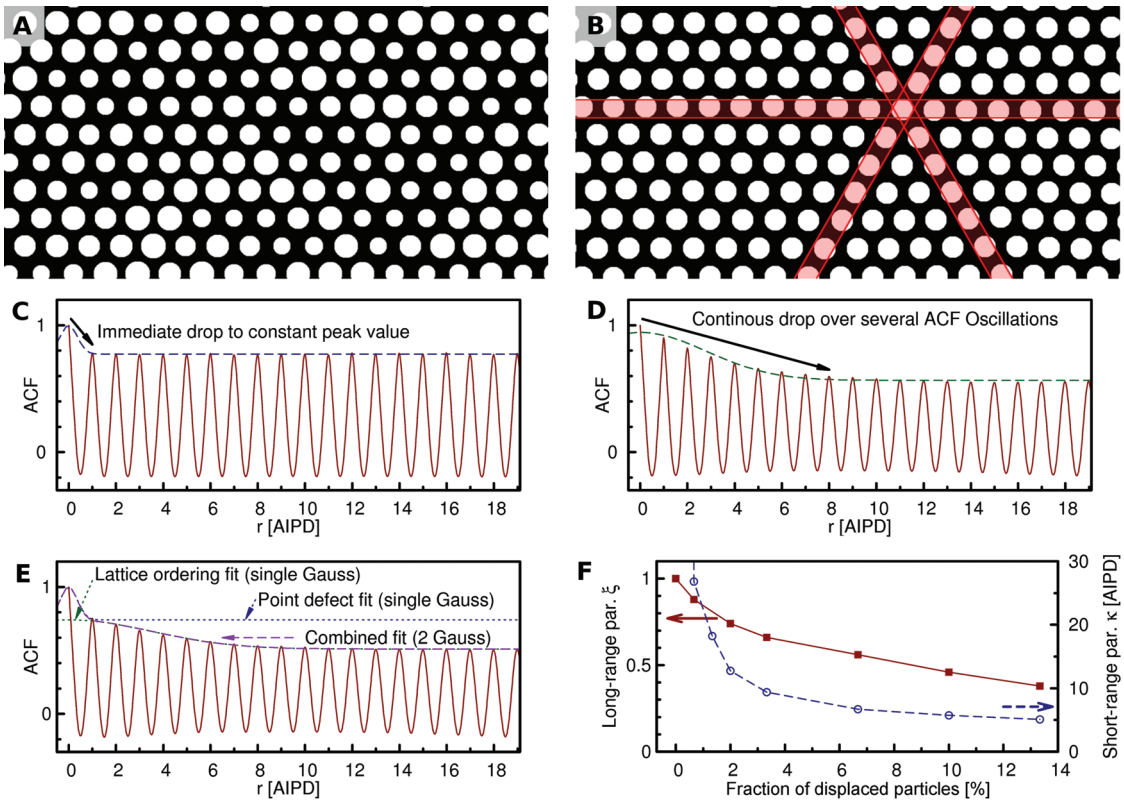

Figure 2. Simulations of model superlattices. (A) Cutout of a polydisperse, well ordered superlattice. (B) Cutout of a monodisperse, but slightly disordered superlattice. (C,D) Line-profiles along a major axis of the simulated 2D-ACFs computed for the images shown in panels A and B and fitted by a Gaussian envelope (dashed line). (E) The line-profiles envelope of a superlattice with polydispersivity and lattice disorder is well fitted by a two Gaussian functions (eq 1). (F) Dependence of the long and short-range parameters ξ_{lr} and κ_{sr} extracted from the ACF analysis as a function of the fraction of displaced particles.

Figures 1A,B exhibit again a hexagonal lattice symmetry, while that of the square superlattice in Figure 1C shows a square symmetry.

The maximum amplitude in the 2D-ACFs is always located in the image center ($|\mathbf{r}| = 0$) and for ordered structures neighboring satellite maxima are found in directions (anti)parallel to the main axes of the superlattice, at a distance from the origin equal to the average interparticle distance (AIPD), which corresponds to the lattice constant *G*. The first order satellite peaks determine the unit cell for the whole ACF lattice as indicated by the shaded areas in Figures 1D−F. Line-profiles along the main axis of the 2D-ACFs in Figure 1 (indicated by dashed lines) show different features for each of the lattice types. For all of them the ACFs are periodic with a period given by the AIPD (which in the case of binaries is defined as distance between two major particles, thus again giving *G*). The line-profiles of the binary superlattices may show additional satellite peaks in between the main peaks due to the different constituents (insets of Figure 1 panels E and F), as will be discussed further below. In all of the line-profiles a decay of the ACF peak heights with increasing distance *r* is observed due to deviations from a perfect ordering induced by various lattice imperfections. Thus, the rate of decay of the ACF envelope is a measure for the imperfectness of the lattice structure, which can be used to quantify the quality of NC superlattices. To obtain a quantitative understanding of relations between lattice imperfections and decay of the ACFs, in the following the ACFs of various simulated NC superlattices are discussed, with imperfections artificially introduced in a well-controlled way.

Simulations and Qualitative Considerations for Single Component Superlattices. Simulated model lattices provide the possibility to deliberately introduce different types of lattice imperfections separately to a perfect lattice. The analysis of their effect on the decay of the ACF at increasing *r* allows us to distinguish two general types of imperfections: (a) local point defect-type imperfections which affect only one individual building block at one particular site. This includes polydispersivity, shape variations, contrast differences, and lattice voids; and (b) lattice distortions that not only affect the position of one single building block, but also their surrounding region. An example is a displacement of a building block from its perfect lattice site that also induces a short-range or even long-range displacement of the surrounding building blocks. To study the effects of these imperfections on the ACFs we use simulated superlattice structures consisting of 1502 hexagonally ordered spherical particles with radius *R* at

5/17 of the lattice constant G. In the first case polydispersivity is introduced by statistically varying R by ±20% (a cutout of the lattice is shown in Figure 2A). In the second case lattice distortions are introduced to a superlattice of monodisperse particles by shifting 7% of the particles by up to 6/5R (see Figure 2B) from their perfect lattice position, which also changes the positions of all other particles by some fraction of the initial displacement with an exponential decay with increasing distance to the originally displaced particle. The straight, shaded bars in Figure 2B indicate the main axes of a perfect hexagonal lattice from which the actual particle positions slightly deviate.

The different nature of imperfections in Figure 2 panels A and B are clearly revealed by their ACF profiles shown in Figures 2 panels C and D, respectively. Evidently, the envelopes of the AC peaks along the chosen major axis of the hexagonally ordered ACF patterns exhibit characteristic decays that strongly depend on the type of lattice imperfections. Polydispersivity (size dispersion) causes an immediate drop of the ACF envelope after one AIPD (*i.e.*, at r equal to one lattice constant G), whereas for larger shifts r, the ACF peak amplitude stays constant due to the long-range ordered particle arrangement (Figure 2C). For longer ranged lattice distortions, in contrast, the envelope of the ACF gradually decays with increasing shift r (see Figure 2D) and only asymptotically approaches a constant value due to the assumed long-range ordering. In experimental NC assemblies, usually both type of imperfections, local pointlike and lattice distortions are present. Therefore, contributions from both effects will be superpositioned in their 2D-ACFs. The fundamentally different decay manner (immediate *vs* continuous and gradual) allows us to distinguish between those two contributions. This is demonstrated by the ACF profile depicted in Figure 2E obtained for a modeled superlattice with the same polydispersivity as the structure of Figure 2A as well as the same disorder due to lattice distortions as in Figure 2B.

In general, for nonperiodic signals $s(\mathbf{x})$, the ACF decays in the form of a Gaussian function. In the case of a periodic signal, the same function can be applied to fit the decay of the ACF(r) peak envelopes (Figure 2C, D). To take into account both polydispersivity as well as lattice distortions, a two-Gaussian function has to be applied (Figure 2E):

$$\mathrm{ACF}_{\mathrm{fit}}(r) = A_\infty + f_0 \exp\left(-\frac{1}{2}(r/\sigma_0)^2\right) + f \exp\left(-\frac{1}{2}(r/\sigma)^2\right) \quad (1)$$

The first Gaussian, characterized by the amplitude f_0, and a fixed width $\sigma_0 = {}^1/_3$ AIPD is ascribed to local, pointlike defects. Even though in principle f_0 would be a measure for abundance of these defects, different contributions like nonuniformities in shape and density of voids or contrast variations due to imaging conditions cannot be distinguished. While these defects contribute to the first drop of the envelope function, the drop itself does not indicate any reduced ordering of the superstructures. The parameters σ and f of the second Gaussian as well as the asymptotic peak level A_∞ to which the peak envelope converges, are characteristic for the short-range and long-range ordering in the assembly. Good long-range ordering is indicated by a small strength f of the second Gaussian as well as a high peak level A_∞ at $r \to \infty$. To characterize long-range ordering quality we suggest the use of the ratio

$$\xi_{\mathrm{lr}} = A_\infty/(f + A_\infty) \quad (2)$$

as the relevant order parameter, giving a value of $\xi_{\mathrm{lr}} = 1$ for perfectly ordered superlattices and $\xi_{\mathrm{lr}} = 0$ for superlattices with no long-range ordering present. In addition a second order parameter κ_{sr} characteristic for the short-range ordering is introduced. Based on the width σ of the second Gaussian in eq 1 the rate of decay of the Gaussian function gives the effective short-range ordering parameter defined as

$$\kappa_{\mathrm{sr}} = \sigma(f + A_\infty)/f \quad (3)$$

When there is no long-range ordering present ($A_\infty = 0$), the effective short-range ordering parameter κ_{sr} is identical to σ, while in the limit of perfect long-range ordering ($f \to 0$), the effective short-range ordering parameter κ_{sr} approaches infinity, indicating the transition from short- to long-range ordering.

To demonstrate the sensitivity of these two parameters on disorder of the superlattice, they were computed from the ACF of the model lattice depicted given in Figure 2B. In this case, the long-range ordering parameter reaches a level of $\xi_{\mathrm{lr}} = 0.56$, whereas the short-range order parameter is $\kappa_{\mathrm{sr}} = 6.7$ AIPD. Varying the number of displaced particles over a wide range from 0 to 13%, the order parameters ξ_{lr} and κ_{sr} increase continuously with a decreasing number of displaced particles. For only 1% of shifted particles values of $\xi_{\mathrm{lr}} = 0.86$ and $\kappa_{\mathrm{sr}} = 23.3$ AIPD are obtained (Figure 2F). This shows how sensitive ξ_{lr} and κ_{sr} depend on disorder of the superlattice structures, and furthermore these values represent an upper limit of what could eventually be obtained for experimental NC-superlattices. Moreover, a fit of the short-range parameter shows that it converges to a value of $\kappa_{sr} \approx \sigma = 3.3$ AIPD for highly disordered systems. This is very close to the coefficient of the exponential decay of the particle displacement used for the construction of the distorted model lattices. In fact, the σ value obtained from the ACF fit is a direct measure for the average lateral extend of the lattice distortions.

Real Nanocrystal Superlattices—Anisotropy. When the ACF analysis is applied to experimentally obtained NC superlattices, directional anisotropies in the superstructures also can be an important issue. In

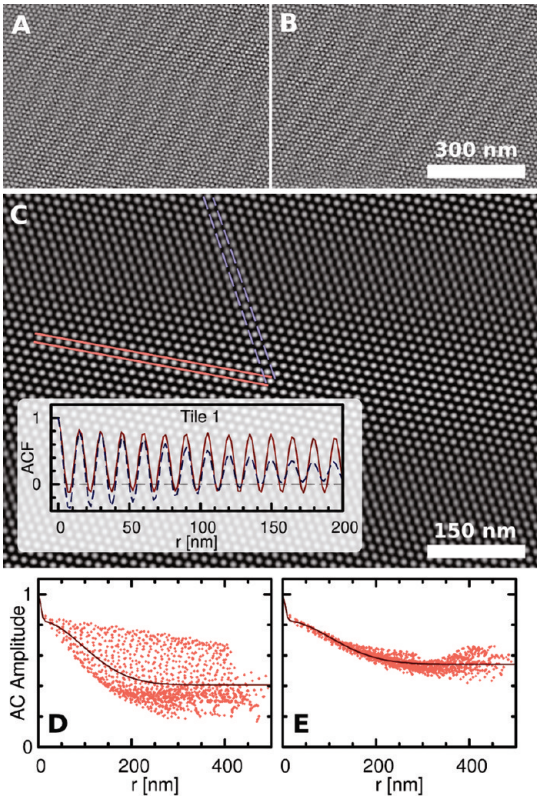

Figure 3. (A, B) Scanning electron micrographs of two different regions of a 11 nm W/C-NC superlattice deposited *via* doctor blade casting (same sample but different locations). (C) The 2D-ACF of image A shows less pronounced ACF peaks in the vertical direction than in the horizontal direction. The inset shows two ACF line-profiles along the two major axes as indicated by the dashed and solid lines in panel C. The dashed line for the vertical direction shows a much stronger and more rapid decay of the ACF peak height than the solid ACF profile for the horizontal direction. (D,E) Plot of all peak heights in the ACF images of A and B as a function of their distance |r| from the center of the 2D-ACF ($r = 0$).

the following, single component superlattices of 11 nm W/C-NCs deposited by doctor blade casting on platinum-coated silicon substrates are discussed. Two highly ordered regions of the same sample, each covered by approximately 2500 NCs, are shown in the scanning electron micrographs in Figure 3 panels A (tile 1) and B (tile 2).

The 2D-ACF of tile 1 (Figure 3C) shows a distinct anisotropy, where apparently the degree of ordering is higher in the horizontal direction than in the vertical direction. This results in less pronounced autocorrelation peaks in the vertical direction. Line-profiles along two major lattice directions, indicated by the dashed and solid lines in the ACF are shown in the inset of Figure 3C to underline this observation. Evidently, the line-profile along the nearly vertical direction (blue, dashed line) shows a decrease of the autocorrelation peak height to a value 0.35 at $r = 150$ nm while the line-profile along the nearly horizontal direction (red, solid line) only drops to a value of 0.7 for the same distance r. Therefore, a 1D analysis of the ACF image along only one direction would deliver an incomplete picture of the lattice quality. For a comprehensive analysis, all directions of the lattice must be treated equally and all peaks found in the ACF image should be included. Here an automated approach, based on a simple algorithm searching for the local, smooth and well isolated peak maxima in the 2D matrix of the ACF in all directions is used (the algorithm for MATLAB as well as detailed description of the procedures is given in the Supporting Information section) to obtain the ACF peak height *versus* the correlation distance r. For the micrographs of the W/C-NC superlattice of Figure 3 panels A and B, the resulting data set is shown in Figure 3 panels D and E, respectively. Evidently, the data points for tile 1 are scattered out much more widely compared to that of tile 2, indicating a much higher anisotropy in the ordering along different directions. A 1D two-Gauss fit over all data points according to eq 1 is used to obtain the average short- and long-range order parameter as well as to quantify the anisotropy of the superlattice. For an anisotropic degree of ordering, the ACF peak values (acv_i) for a certain distance r vary along different directions. The average squared residual per data point acv_i with respect to the value of the fit function ACF_{fit} characterizes the degree of anisotropy in ordering:

$$a = \sqrt{\frac{1}{n}\sum_{i}^{n}(acv_i - ACF_{fit}(r_i))^2} \qquad (4)$$

where the index i runs over all data points, that is, the ACF maxima acv_i.

Since for a 1D-fit of a 2D data set, the longer distances are overrepresented by a larger number of data points at larger r_i, a $1/r$ weighting of the data points is introduced, which leads to a balanced fit for the short range as well as for the long-range data points. The fits are indicated by the solid lines in Figures 3 panels D and E, all showing an initial drop in the first AIPD due to pointlike defects and a continuous, gradual decay of the peak heights due to lattice distortions. The actual results derived from the fit of the data using eq 1−4 give a long-range parameter $\xi_{lr} = 0.49$ and 0.65 for tile 1 and 2, respectively. Much more significant, however, is the difference of a factor of 4 in anisotropy, giving $a = 0.034$ for tile 2 and $a = 0.135$ for tile 1. This is evidence of the high sensitivity of a in respect to the anisotropy of ordering.

Comparison of Various Single Component Superlattices. In the following, the quality of ordering of three different experimentally obtained single component superlattices is quantitatively compared: The samples comprise, on the one hand, two colloidal NC superlattices, a 18.8 nm In NC superlattice prepared by drop casting (Figure 4A) and a 20 nm W/C NC superlattice prepared

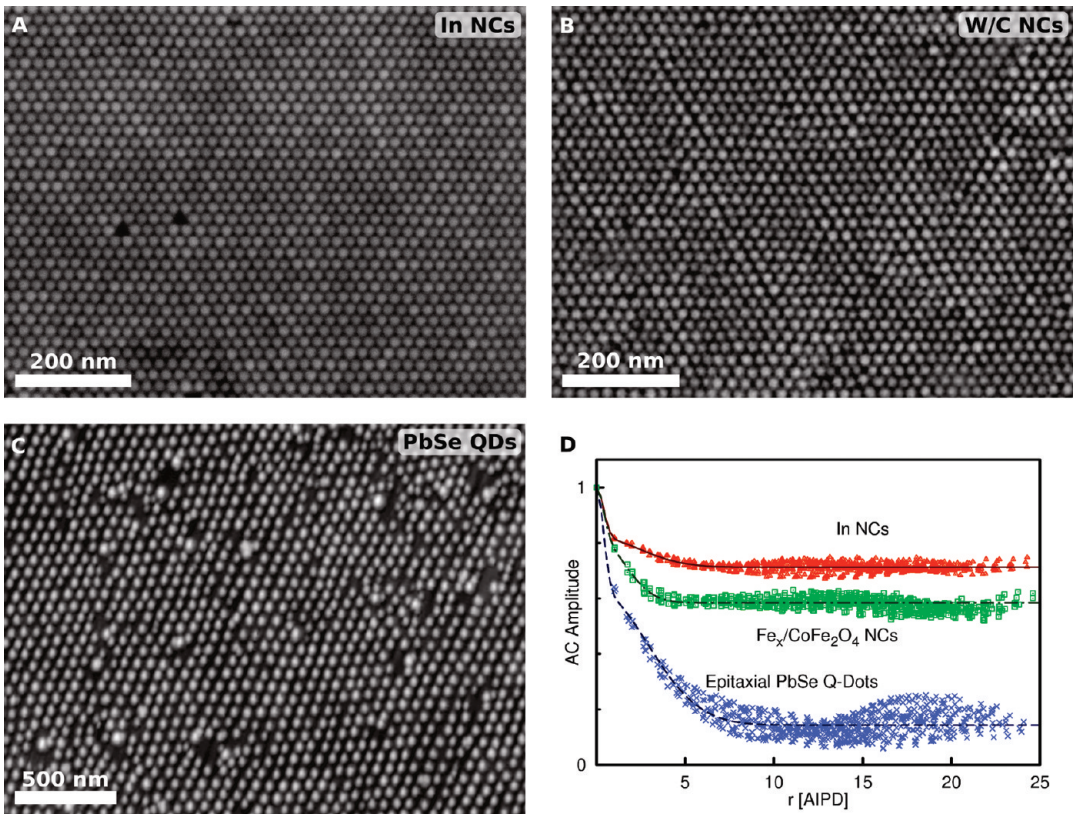

Figure 4. Micrographs of experimental self-assemblies of different building blocks. (A) Drop casted 18.8 nm indium nanocrystal SL with exceptionally high ordering. (B) Doctor blade cast 20 nm W/C-NC SL, where short-range wiggles disturb the ordering. (C) Top most layer of an epitaxially grown PbSe/Pb$_{1-x}$Eu$_x$Te QD SL, exhibiting a three-dimensional face centered cubic quantum dot ordering. (D) Comparison of the decay of the 2D-ACF peak heights obtained for the images in A−C. Dashed, dot−dashed, and solid lines represent fits according to eq 1.

by doctor blade casting (Figure 4B), and, on the other hand, an ordered array of epitaxial PbSe quantum dots in a Pb$_{1-x}$Eu$_x$Te matrix (Figure 4C), prepared by molecular beam epitaxy.[4−6] Figure 4C represents the atomic force microscopy image of the topmost layer of the corresponding three-dimensional ordered quantum-dot crystal in which the PbSe dots are arranged in a trigonal lattice with a face-centered cubic (fcc)−like A−B−C−A−B−C vertical stacking sequence and in which the lateral ordering of the dots progressively increases with an increasing number of deposited superlattice periods. Owing to the strong and anisotropic elastic interactions between the PbSe dots these superlattices represent the best spontaneously ordered epitaxial self-assemblies of quantum dots reported in literature.[4−6]

For a consistent comparison of the ordering in these totally different systems, a systematic procedure is required. The characteristic parameters ξ_{lr}, κ_{sr}, and a not only depend on the chosen area of the investigated NC assemblies but also require a sufficiently large number of assembled particles in the areas under investigation. Also, a minimum resolution (pixels/AIPD) is mandatory, to account for small changes of the individual particle positions. Thus a standard protocol has to be applied to obtain a reliable comparison between the various different systems. In the following we use a standard micrograph size of 800 × 600 pixels for the different samples and the magnification is chosen such that one AIPD corresponds to 20 pixels/AIPD, regardless of the physical dimensions of the self-assembled particles. In the case of hexagonal ordered superlattices this corresponds to micrographs covering about 1000 building blocks as shown in Figure 4A−C. From these images the 2D-ACFs are computed with the help of a scanning probe microscopy analyzing software, and the ACF peak values and positions are extracted from the ACF matrix data by the MATLAB program provided in the Supporting Information section. The obtained data are summarized in Figure 4D. Evidently the In NC superlattice (red triangles) shows

TABLE 1. List of Short and Long-Range Ordering as Well as Anisotropy Parameters ξ_{lr}, κ_{sr}, and a Derived for the Single Component In NC, W/C NC, and Epitaxial PbSe QD Superlattices Presented in Figure 4 and the Binary CdSe/PbS NC Superlattice Presented in Figure 5

	indium NCs	W/C NCs	epitaxial PbSe QDs	binary CdSe/PbS NCs
long-range ξ_{lr}	0.86	0.71	0.22	0.74
short-range κ_{sr} [AIPD]	71	11	7.5	62
anisotropy a	0.014	0.021	0.041	0.034

the best long-range ordering, better than the W/C NC superlattice (green squares) and by far better than for the epitaxial quantum dots (blue crosses). To quantify these statements, the ACF results are fitted and evaluated by eqs 1−4, resulting in the characteristic order and anisotropy parameters listed in Table 1. The long-range order parameter for the In NCs reaches a value of $\xi_{lr} = 0.87$, corresponding according to Figure 2F to only 1% of slightly shifted NCs. For the epitaxial quantum dot system, the same parameter is about 4 times smaller and the residual AC peak amplitude A_∞ at large r is much smaller, clearly evidencing that the ordering of colloidal NCs with small size dispersion outperforms that obtained by epitaxial growth. The differences between the self-assembly of the two relatively similar NC systems shown in Figure 4 panels A and B can also be quantified. The long-range order parameter for the W/C-NCs is found to be only 18% worse than that of the In NCs, whereas the anisotropy is two times worse. Additionally, the small short-range wiggles present in the SEM image of the W/C NC superlattice (Figure 4B) result in a reduced short-range ordering. Thus, the corresponding short-range order parameter κ_{sr} is by 84% lower than for the In NC superlattice.

Analyzing Autocorrelation Functions of Binary Superlattices. Naturally, the analysis of the ACF of binary superlattices is more involved than those of single component ones. The most obvious differences are the appearance of satellite peaks in between the main peaks in the 2D-ACF, as already highlighted in the discussion of Figure 1. To understand this feature again a model superlattice is studied. A cutout of the model, which consists of approximately 2500 particles of two sizes is illustrated in Figure 5A. Simulated polydispersivity and lattice distortions are also introduced for both particle sizes in the same way as for the simulated single component superlattices. As described above, the ACF corresponds to the self-correlation of the structure at various displacements r. At a particular shift of $r = {}^1/_2$ AIPD, where here 1 AIPD is the average distance between two big particles, the big particles of the shifted binary superlattice lie over two small particles of the unshifted ones. This situation is sketched in Figure 5B, where the shifted particles are shown by the dashed lines. At this shift, the ACF exhibits an intermediate peak, whereas for a shift of $r = 1$ AIPD the ACF shows a main peak. The corresponding line-profile along one major axis of the autocorrelation pattern (Figure 5C) resembles quite well the one of the binary nanocrystal superlattices (W/C-NCs combined with gold nanocrystals) shown in the inset of Figure 1E. The first intermediate and main peaks in the ACF line-profile are indicated by small arrows. For analyzing the decay of the ACF, only the main peaks have to be taken into account. The autocorrelation main peaks again can be fitted adequately with eq 1 as found for the single component

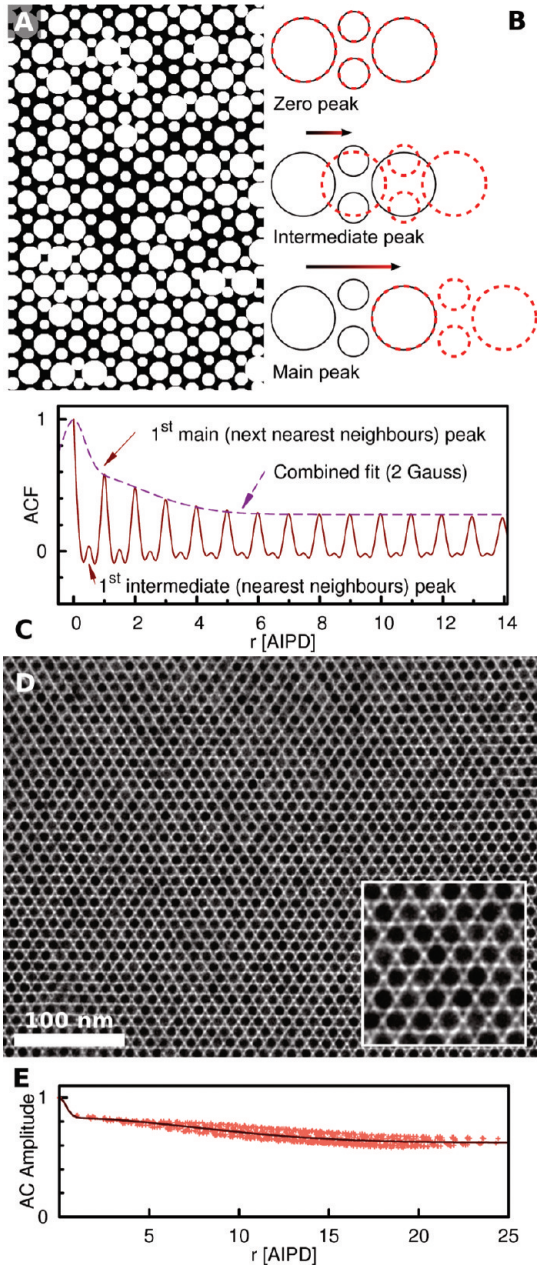

Figure 5. (A) Simulated binary superlattice resembling the W/C−Au binary nanocrystal superlattice from Figure 1B. Polydispersivity and lattice distortions are introduced for both, the big and the small particles. (B) Schematic illustration of the autocorrelation overlap for $r = 0$, ${}^1/_2$ and 1 AIPD. At a $r = {}^1/_2$ AIPD the big particle overlaps with two small particles, hence leading to a small, intermediate peak in the ACF. (C) A line-profile along a major axis of the computed ACF shows main and intermediate ACF peaks, a fit to the main peaks according to eq 1 is shown as dashed line. (D) TEM image of an experimental binary NC superlattice containing 8 nm CdSe NCs and 3.1 nm PbS NCs, AlB_2 structure. (E) The envelope fit to the 2D-ACF peaks evidencing very good short-range and long-range ordering.

NC superlattices. The symmetry of the superlattice under investigation does not play a role in the analysis.

To enable a comparison of the quality of ordering in binary superlattices with those obtained in the single component ones, again the same micrograph size and

resolution has to be employed. The analysis is applied to the superlattice shown in Figure 5D obtained upon drying from a mixture of 8 nm CdSe and 3.1 nm PbSe NCs from solution. Remarkably, not a single point defect is present in the TEM micrograph and ordering seems to be nearly perfect over the whole sample. The fit of the decay of the ACF peak envelope, shown in Figure 5E, gives an as good long-range order parameter ξ_{lr} as for the single component W/C superlattice and an short-range parameter κ_{sr} close to the one obtained for In NC superlattice (see Table 1). Thus, the quality of ordering obtained in binary NC superlattice structures can be as good as in single component ones. For the binary NC structure in Figure 5D only the anisotropy parameter *a* is slightly worse than those obtained for the single component ones.

CONCLUSION

For quantifying the ordering in self-assembled nanoscale superstructures a procedure is proposed based on the analysis of the 2D-autocorrelation function of microscopy images. Fitting the characteristic decays of the ACF peak envelopes *versus* distance by a two-Gauss function allows the extraction of characteristic long- and short-range order parameters, as well as the anisotropy of ordering. With these three parameters, it is possible to quantitatively compare different superlattice structures, single component and binary NC assemblies, and even epitaxial quantum dot superstructures. Application of the analysis to several material systems and self-assembly processes evidence a better ordering in NC superlattices from colloidal solution than in epitaxial quantum dot systems. Because of the high sensitivity of the autocorrelation to lattice distortions compared to previously used statistical evaluation methods for colloidal self-assemblies, our presented method allows us to reveal even small differences between superlattices of almost the same ordering quality, which are not apparent by visual inspection of the microscopy images. Moreover, in contrast to the previously methods, determination of the exact particle positions is not necessary in our approach. Therefore, our analysis method presents a straightforward and easy to use tool, allowing comprehensive quantitative comparisons of the ordering present in self-assembled superstructures.

EXPERIMENTAL SECTION

Synthesis of $Fe_xO/CoFe_2O_4$, PbS, Au, and In NCs. $Fe_xO/CoFe_2O_4$ core−shell NCs of 11 and 22 nm capped with oleic acid were synthesized by thermal decomposition of mixtures of metal oleates in high-boiling organic solvents, as described previously.[34] Au NCs (∼5.5 nm) were prepared *via* digestive ripening process,[25,35] using $AuCl_3$ as precursor, $NaBH_4$ as reducing agent and dodecanethiol as stabilizer. Oleic-acid capped PbS NCs (∼5 and 3.1 nm) were prepared according to Hines *et al.*[36] from lead oleate and bis-(trimethylsilyl)sulfide; 4.6 nm PbSe NCs were synthesized from $PbCl_2$ and TOPSe in oleylamine according to ref 37. CdSe nanocrystals (8 nm) were synthesized according to ref 38 from dimethylcadmium and TOPSe in mixture of hexadecylamine, trioctylphosphine oxide, and trioctylphosphine. Oleic-acid capped In NCs (18.8 nm) were synthesized by the reduction of an indium organometallic compound in nonpolar solvents. This novel procedure will be published elsewhere.

Preparation of NC Superlattices by Doctor-Blade Casting and Drop-Casting. Well-purified NCs were dissolved in chlorobenzene or tetrachloroethylene at a concentration of $\sim 10^{14}$ cm^{-3}. Oleic acid was added to this solution up to a concentration of 1−2 μg cm^{-3}. Colloidal solutions of W/C-NCs were cast onto the Si (or Pt-coated Si) substrates at 60 °C using a commercial coater from Erichsen GmbH (Coatmaster 509/MC-I). The Si substrates were freshly hydrophobized by dipping into HF or by a standard treatment with hexamethyldisilane. Further details can be found in ref 16.

Growth of Binary NC Superlattices. Carbon-coated TEM grids (Ted Pella, Type-B) were placed into a tilted glass vial (∼60° tilt angle). A ∼20−25 μL portion of a solution containing two kinds of NCs in the desired particle number ratio at the concentration of $\sim 10^{14}$ NCs/cm^{-3}. TCE was used as a solvent. The solvent was evaporated for 5 h at ∼50 °C under nitrogen atmosphere.

Growth of Epitaxial Quantum Dot Superlattice. Epitaxial PbSe QDs were grown by Stranski−Krastanov growth on PbEuTe using molecular beam epitaxy. The superlattice consists of 60 periods of five monolayers of PbSe (111) oriented alternating with 48 nm PbEuTe spacer layers, resulting in an fcc-like stacking and hexagonal lateral ordering as described in refs 4 to 6.

Structural Characterization of NC Superlattices. The single component NC superlattices were imaged by a Zeiss Cross Beam 1540 scanning electron microscope and the binary NC superlattices by transmission electron microscopy using a FEI Technai F3 microscope operated at an acceleration voltage of 300 kV. The TEM images were compared to the BNSL projections simulated using Accelrys MS Modeling 4 and Crystal Maker 1.4 software packages.

Processing of Images. For the autocorrelation analysis only the topmost layer of the deposited nanocrystals is analyzed. Underlying material (*e.g.*, accumulated excess of stabilizer or islands of nanocrystals) appear as darker shaded areas in SEM images. These areas have to be removed without affecting the information on the ordering of NCs in the topmost layer. This is performed *via* a subtraction of a Gaussian blurred image of the original image from the original image using the GNU Image Manipulation Program (GIMP). Details of this procedure can be found in ref 16.

Simulation of Superlattices. Simulation of the superlattices was performed by using the GNU Octave numerical computing language. First a 2D-matrix of 2300 × 2000 zero valued pixels was defined and the coordinates of a perfectly hexagonally ordered superlattice within this matrix were calculated. The particles themselves consisted of matrices of 49 × 49 zero valued pixels. These matrices were filled from their center to a desired radius by pixels with a value of 1. The basic radius was 20 pixels; for the polydispersivity simulations a set of matrices ranging from radii of 16−24 pixels were defined. For the distorted superlattices, a random displacement of a particle position was introduced, which affected the position of all other particle position by some fraction of the initial displacement. This fraction is chosen to decrease exponentially with distance from the initially displaced particles. This process was repeated several times to affect the desired number of particles. By simply adding the sets of particle matrices to the basic matrix at the perfect as well at the distorted particle positions, four different superlattices could be constructed: a monodisperse, well ordered SL, a polydisperse well ordered SL, a monodisperse distorted SL, and a polydisperse distorted SL. The latter three were used in this work. For the simulated binary crystal, a different basic arrangement was used for the particle positions. The different particle sizes arose from the usage of two sets of particle sizes with different basic radii.

Autocorrelation Analysis. The autocorrelation analysis was performed using the Gwyddion scanning probe microscopy analyzing software. The zero level was defined to be at the mean value of the image before the calculation of the autocorrelation function. The line-profiles and 2D-correlograms were exported as ASCII files for further processing. The GNU Octave software package was used to normalize the line-profiles and correlograms to their maximum value at $\mathbf{r} = 0$. For both, a routine finding the maxima and hence the peaks in the autocorrelation functions was performed on the data and stored in dependence of their distance from the central peak at $\mathbf{r} = 0$. A two Gauss function was then defined in the Gnuplot software and $1/r$-weight-fitted *via* the least-squares method to the data, delivering the parameters necessary for the quantification of the ordering.

Acknowledgment. This work was supported by the Austrian Nano-Initiative (project NSI) and by the Austrian Science Fund FWF (project START 179 and SFB IRON). We thank O. Fuchs for technical support.

Supporting Information Available: The calculation of a 2D autocorrelation function of a 2D data set is discussed and illustrated in Figure S1. Furthermore, a detailed description of the analysis of the autocorrelation function using numerical mathematical software as well as readily available software packages, including the source for a program searching for maxima in the ACF peak patterns, is given. This material is available free of charge *via* the Internet at http://pubs.acs.org.

REFERENCES AND NOTES

1. Pileni, M.-P. *Nanocrystals Forming Mesoscopic Structures*; Pileni, M.-P., Ed.; Wiley VCH: Weinheim, Germany, 2005.
2. Azzaroni, O.; Fonticelli, M.; Schilardi, P. L.; Benítez, G.; Caretti, I.; Albella, J. M.; Gago, R.; Vázquez, L.; Salvarezza, R. C. Surface Nanopatterning of Metal Thin Films by Physical Vapour Deposition onto Surface-Modified Silicon Nanodots. *Nanotechnology* **2004,** *15*, 197–200.
3. Martin, J. I.; Nogues, J; Liu, K.; Vicent, J. L.; Schuller, I. K. Ordered Magnetic Nanostructures: Fabrication and Properties. *J. Magn. Magn. Mater.* **2003,** *256*, 449–501.
4. Springholz, G.; Holy, V.; Pinczolits, M.; Bauer, G. Self-Organized Growth of Three- Dimensional Quantum-Dot Crystals with fcc-like Stacking and a Tunable Lattice Constant. *Science* **1998,** *282*, 734–737.
5. Pinczolits, M.; Springholz, G.; Bauer, G. Evolution of Hexagonal Lateral Ordering in Strain-Symmetrized PbSe/$Pb_{1-x}Eu_xTe$ Quantum-Dot Superlattices. *Phys. Rev. B.* **1999,** *60*, 11524–11529.
6. Springholz, G.; Pinczolits, M.; Holy, V.; Zerlauth, S.; Vavra, I.; Bauer, G. Vertical and Lateral Ordering in Self-Organized Quantum Dot Superlattices. *Phys. E* **2001,** *9*, 149–163.
7. Tersoff, J.; Teichert, C.; Lagally, M. G. Self-Organization in Growth of Quantum Dot Superlattices. *Phys. Rev. Lett.* **1996,** *76*, 1675–1678.
8. Liu, F.; Davenport, S. E.; Evans, H. M.; Lagally, M. G. Self Organized Replication of 3D Coherent Island Size and Shape in Multilayer Heteroepitaxial Films. *Phys. Rev. Lett.* **1999,** *82*, 2528–2531.
9. Ortner, G.; Bayer, M.; Larionov, A.; Timofeev, V. B.; Forchel, A.; Lyanda-Geller, Y. B.; Reinecke, T. L.; Hawrylak, P.; Fafard, S.; Wasilewski, Z. Fine Structure of Excitons in InAs/GaAs Coupled Quantum Dots: A Sensitive Test of Electronic Coupling. *Phys. Rev. Lett.* **2003,** *90*, 86404/1–86404/4.
10. Murray, C. B.; Kagan, C. R.; Bawendi, M. G. Synthesis and Characterization of Monodisperse Nanocrystals and Close-Packed Nanocrystal Assemblies. *Annu. Rev. Mater. Sci.* **2000,** *30*, 545–610.
11. Lin, X. M.; Jaeger, H. M.; Sorensen, C. M.; Klabunde, K. J. Formation of Long-Range-Ordered Nanocrystal Superlattices on Silicon Nitride Substrates. *J. Phys. Chem. B* **2001,** *105*, 3353–3357.
12. Bigioni, T. P.; Lin, X.-M.; Nguyen, T. T.; Corwin, E. I.; Witten, T. A.; Jaeger, H. M. Kinetically Driven Self-Assembly of Highly Ordered Nanoparticle Monolayers. *Nat. Mater.* **2006,** *5*, 265–270.
13. Coe-Sullivan, S.; Steckel, J. S.; Woo, W. K.; Bawendi, M. G.; Bulovic, V. Large-Area Ordered Quantum-Dot Monolayers *via* Phase Separation During Spin-Casting. *Adv. Funct. Mater.* **2005,** *15*, 1117–1124.
14. Collier, C. P.; Saykally, R. J.; Shiang, J. J.; Henrichs, S. E.; Heath, J. R. Reversible Tuning of Silver Quantum Dot Monolayers through the Metal-Insulator Transition. *Science* **1997,** *277*, 1978–1981.
15. Aleksandrovic, V.; Greshnykh, D.; Randjelovic, I.; Frömsdorf, A.; Kornowski, A.; Roth, S. V.; Klinke, C.; Weller, H. Preparation and Electrical Properties of Cobalt−Platinum Nanoparticle Monolayers Deposited by the Langmuir−Blodgett Technique. *ACS Nano* **2008,** *2*, 1123–1130.
16. Bodnarchuk, M. I.; Kovalenko, M. V.; Pichler, S; Fritz-Popovski, G.; Hesser, G.; Heiss, W. Large-Area Ordered Superlattices from Magnetic Wüstite/Cobalt Ferrite Core/Shell Nanocrystals by Doctor Blade Casting. *ACS Nano* **2010,** *4*, 423–431.
17. Siffalovic, P.; Majkova, E.; Chitu, L.; Jergel, M.; Luby, S.; Capek, I.; Satka, A.; Timmann, A.; Roth, S. V. Real-Time Tracking of Superparamegnetic Nanoparticle Self-Assembly. *Small* **2008,** *4*, 2222–2228.
18. Siffalovic, P.; Majkova, E.; Chitu, L.; Jergel, M.; Luby, S.; Satka, A.; Roth, S. V. Self-Assembly of Iron Oxide Nanoparticles Studied by Time-Resolved Grazing-Incidence Small Angle X-ray Scattering. *Phys. Rev. B* **2007,** *76*, 195432/1–195432/8.
19. Jiang, Z.; Lin, X.-M.; Sprung, M.; Narayanan, S.; Wang, J. Capturing the Crystalline Phase of Two-Dimensional Nanocrystal Superlattices in Action. *Nano Lett.* **2010,** *10*, 799–803.
20. Redl, F. X.; Cho, K. S.; Murray, C. B.; O'Brien, S. Three-Dimensional Binary Superlattices of Magnetic Nanocrystals and Semiconductor Quantum Dots. *Nature* **2003,** *423*, 968–971.
21. Talapin, D. V.; Lee, J.-S.; Kovalenko, M. V.; Shevchenko, E. V. Prospects of Colloidal Nanocrystals for Electronic and Optoelectronic Applications. *Chem. Rev.* **2010,** 389–458.
22. Burda, C.; Chen, X.; Narayanan, R.; El-Sayed, M. A. Chemistry and Properties of Nanocrystals of Different Shapes. *Chem. Rev.* **2005,** *105*, 1025–1102.
23. Chen, Z.; O'Brien, S. Structure Direction of II-VI Semiconductor Quantum Dot Binary Nanoparticle Superlattices by Tuning Radius Ratio. *ACS Nano* **2008,** *2*, 1219–1229.
24. Shevchenko, E. V.; Talapin, D. V.; Kotov, N. A.; O'Brien, S.; Murray, C. B. Structural Diversity in Binary Nanoparticle Superlattices. *Nature* **2006,** *439*, 55–59.
25. Kalsin, A. M.; Fialkowski, M.; Paszewski, M.; Smoukov, S. K.; Bishop, K. J. M.; Grzybowski, B. A. Electrostatic Self-Assembly of Binary Nanoparticle Crystals with a Diamond-like Lattice. *Science* **2006,** *312*, 420–424.
26. Shevchenko, E. V.; Talapin, D. V.; Murray, C. B.; O'Brien, S. Structural Characterization of Self-Assembled Multifunctional Binary Nanoparticle Superlattices. *J. Am. Chem. Soc.* **2006,** *128*, 3620–3637.
27. Talapin, D. V.; Shevchenko, E. V.; Bodnarchuk, M. I.; Ye, X.; Chen4, J.; Murray, C. B. Quasicrystalline Order in Self-Assembled Binary Nanoparticle Superlattices. *Nature* **2009,** *461*, 964–967.
28. Overgaag, K.; Evers, W.; de Nijs, B.; Koole, R.; Meeldijk, J.; Vanmaekelbergh, D. Binary Superlattices of PbSe and CdSe Nanocrystals. *J. Am. Chem. Soc.* **2008,** *130*, 7833–7835.
29. Ramos, L.; Lubensky, T. C.; Dan, N.; Nelson, P.; Weitz, D. A. Surfactant-Mediated Two-Dimensional Crystallization of Colloidal Crystals. *Science* **1999,** *286*, 2325–2328.
30. Terao, T.; Nakayama, T. Crystallization in Quasi-Two-Dimensional Colloidal Systems at an Air−Water Interface. *Phys. Rev. E* **1999,** *60*, 7157–7162.
31. Gray, J. J.; Klein, D. H.; Bonnecaze, R. T.; Korgel, B. A. Nonequilibrium Phase Behavior During the Random Sequential Adsorption of Tethered Hard Disks. *Phys. Rev. Lett.* **2000,** *85*, 4430–4433.

32. Shah, P. S.; Novick, B. J.; Hwang, H. S.; Lim, K. T.; Carbonell, R. G.; Johnston, K. P.; Korgel, B. A. Kinetics of Nonequilibrium Nanocrystal Monolayer Formation: Deposition From Liquid Carbon Dioxide. *Nano Lett.* **2003,** *3*, 1671–1675.
33. Kim, B.; Carignano, M. A.; Tripp, S. L.; Wei, A. Cluster Size Analysis of Two-Dimensional Order in Colloidal Gold Nanoparticle Arrays. *Langmuir* **2004,** *20*, 9360–9365.
34. Bodnarchuk, M. I.; Kovalenko, M. V.; Groiss, H.; Resel, R.; Reissner, M.; Hesser, G.; Lechner, R. T.; Steiner, W.; Schaffler, F.; Heiss, W. Exchange-Coupled Bimagnetic Wüsteite/Metal Ferrite Core/Shell Nanocrystals: Size,Shape, and Compositional Control. *Small* **2009,** *5*, 2247–2252.
35. Prasad, B. L. V.; Stoeva, S. I.; Sorensen, C. M.; Klabunde, K. J. Digestive Ripening of Thiolated Gold Nanoparticles: The Effect of Alkyl Chain Length. *Langmuir* **2002,** *18*, 7515–7520.
36. Hines, M. A.; Scholes, G. D. Colloidal PbS Nanocrystals with Size-Tunable Near-Infrared Emission: Observation of Post-Synthesis Self-Narrowing of the Particle Size Distribution. *Adv. Mater.* **2003,** *15*, 1844–1849.
37. Kovalenko, M. V.; Talapin, D. V.; Loi, M. A.; Cordella, F.; Hesser, G.; Bodnarchuk, M. I.; Heiss, W. Quasi-Seeded Growth of Ligand-Tailored PbSe Nanocrystals through Cation-Exchange-Mediated Nucleation. *Angew. Chem.* **2008,** *47*, 3029–3033.
38. Talapin, D. V.; Rogach, A. L.; Kornowski, A.; Haase, M.; Weller, H. Highly Luminescent Monodisperse CdSe and CdSe/ZnS Nanocrystals Synthesized in a Hexadecylamine−Trioctylphosphine Oxide−Trioctylphospine Mixture. *Nano Lett.* **2001,** *1*, 207–211.